Plasma assisted micro poling of glassy surfaces: a new tool to achieve liquid crystal multi-domain alignments [Invited]

Alice Goillot, Alexis Maillard, Tigran Galstian, Younès Messaddeq, Frederic Adamietz, Vincent Rodriguez, Marc Dussauze

Plasma assisted micro poling of glassy surfaces: a new tool to achieve liquid crystal multi-domain alignments

ALICE GOILLOT,[1,2] ALEXIS MAILLARD,[1,2] TIGRAN GALSTIAN,[2] YOUNÈS MESSADDEQ,[2] FREDERIC ADAMIETZ,[1] VINCENT RODRIGUEZ,[1] MARC DUSSAUZE[1,*]

[1]*Institut des Sciences Moléculaires, UMR 5255 CNRS, Université de Bordeaux, 351 cours de la Libération, Talence Cedex 33405, France*
[2]*Centre d'optique, photonique et laser, Department of Physics, 2375 rue de la Terrasse, Université Laval, Québec, G1V 0A6, Canada*

**marc.dussauze@u-bordeaux.fr*

Abstract: We propose an innovative approach to program the alignment of liquid crystal (LC) assemblies allowing for the formation of multi-domain alignments whose orientation axis and sizes are controlled at the micrometer scale by an electrically patterned glass surface. The glass surface preparation is based on a thermo-electrical imprinting process to induce localized space charge implantations in the glass matrix just below its anode surface. To demonstrate this new approach, a commercial soda-lime glass slide has been polarized using as anode a simple micrometric nickel grid. Characterizing the polarized glass surface by second harmonic generation polarized microscopy; we show an accurate control of both location and spatial components of frozen static fields embedded in the glass as a function of the electrode patterns. The polarized glassy surface is then used in the conception of a LC cell in which homeotropic or planar alignments can be controlled following the electrical pattern induced on the glass surface. This study also points out the importance of plasma discharges spatially controlled along the electrode pattern during the process in order to promote the in-plane electrical polarization effects, which are essential for the programming of the in-plane LC alignment on the polarized glass surface.

1. Introduction

Since the beginning of liquid crystal (LC) displays' (LCD) development in the 1960's [1], this field has reached high level of maturity and is now bringing unique possibilities for the development of many other optical devices in photonics such as LCs-based optical attenuators, polarization controllers, phase retarders and waveguides for instance [2]. To control LCs properties, one should manage their orientations that are governed by surface interactions. To do so, rubbing methods are largely adopted by the LC industry, as they permit large scale homogenous LCs ordering [3–5]. To offer new possibilities in the design of LC devices, various top-down fabrication techniques have been successfully developed to modify the orientation of LC assemblies on various surfaces [6]. Most of them are based either on chemical [7–9] or on topological surface patterns to taylor LCs alignments. Among these methods, a large variety of photoalignment processes has been reported. They could be referred to two main different mechanisms among others, first, the irradiation can be used to locally modify the surface chemistry of photosensitive polymers or of a self-assembled monolayers [14–17]. Second, the orientational changes of LCs matrices can be triggered by photochromic molecules, the alignment here is obtained by direct irradiation of the LC mesophase [18–20].
Without going more into technical details about these well documented methods to control the assembly of LC materials, one should point out their growing interest as they open the way to accurate 2D and 3D controls of LC molecular arrangements for innovative properties

and functionalities in many applications. However, most of the described above approaches are using wet processing of surfaces (casting various liquid films on substrates and the further processing to solidify them), which become larger and larger (reaching several meters of diameter for last generation of LCDs). This is dramatically complicating the manufacturing process. In this context, it might be very desirable to have an alignment technique that might provide local orientational patterning capability while avoiding the above-mentioned wet processes.

In this paper, we propose a new approach for multi-domain LC alignment based on the use of a polarized ("poled") glass surface. The basic principle of the glass surface polarization process consists in the application of a high DC voltage to a heated glass substrate in order to induce a depletion of ionic charge carriers, such as alkali cations, in the glassy matrix. Then, the temperature is decreased to freeze the polarized state of the glass before to turn off the DC field. The studies of electrically polarized glassy surfaces have been a topic in the early 1990's with works on second order optical properties in poled silica for photonic applications [21], as well as for anodic bonding in microelectronic applications [22–24]. More recently this kind of DC poling process has been shown to be manageable at the micrometric scale resulting in thermo-electrical micro-imprinting treatments of glass surfaces [25]. When applied to specifically optimized glass compositions, an accurate control of various properties were reported such as optical properties (refractive index [26] and second order optical response [27,28]), surface electrical potential [29] but also chemical properties (durability [30] and surface reactivity [31,32]) and wettability [7].

Following the idea that such methodology allows to pattern surface electrical functions on a large variety of ionic glasses [29,33–35], in this work, we focus our attention on the use of frozen static electric fields patterned in a poled glass substrate to impose a so-called "easy axes" for LCs orientations on its surface. We have characterized the electrical fields' locations and spatial components, patterned on a commercial silicate glass surface, by using Second Harmonic Generation (SHG) polarized microscopy. A clear correlation is demonstrated between the glass surface electrical patterns and both orientations and domain formations of LCs characterized by cross polarization microscopy and polarized Raman imaging. Lastly, we highlight the importance of surface electrical current and plasma discharges during the imprinting polarization process in order to promote long-range in-plane electrical polarization effects, which are essential for a further control of in-plane LCs alignment on the polarized glass surface. We think that this approach can be developed into a step-by-step poling technique that may become a practical tool for modern LC device manufacturing, providing thus better performance and functionalities.

2. Thermo-electrical imprinting process and LC cell preparation

Figure 1 schematically shows various steps of the LC cell preparation which starts from an imprinting thermo-electrical process (**Figure 1 (a)**) to pattern the surface of a commercial soda lime silicate glass (SLG). The polarization treatment was done at 250 °C with a voltage of 1400 V during 30 min under nitrogen atmosphere. The anode configuration governing the final electrical pattern on the glass surface is a nickel grid having a thickness of 4µm and composed of 10 µm wide wires forming 40 µm wide squares. To finalize the treatment, the temperature is decreased to room temperature, the voltage is turn off and the poled SLG surface is extracted (**Figure 1 (b)**) in order to be used in the conception of a LC cell (**Figure 1 (c)**). The poled substrate is assembled with another SLG glass that was coated with a homeotropic polyimide polymer (PI) using a UV curing glue and silica balls as spacers to constitute a 5 µm thick LC cell (**Figure 1(c)**). The cell is then filled with the LC composition 4'-hexyl-biphenylcabonitrile (**Figure 1(d)**), sold by Merck.

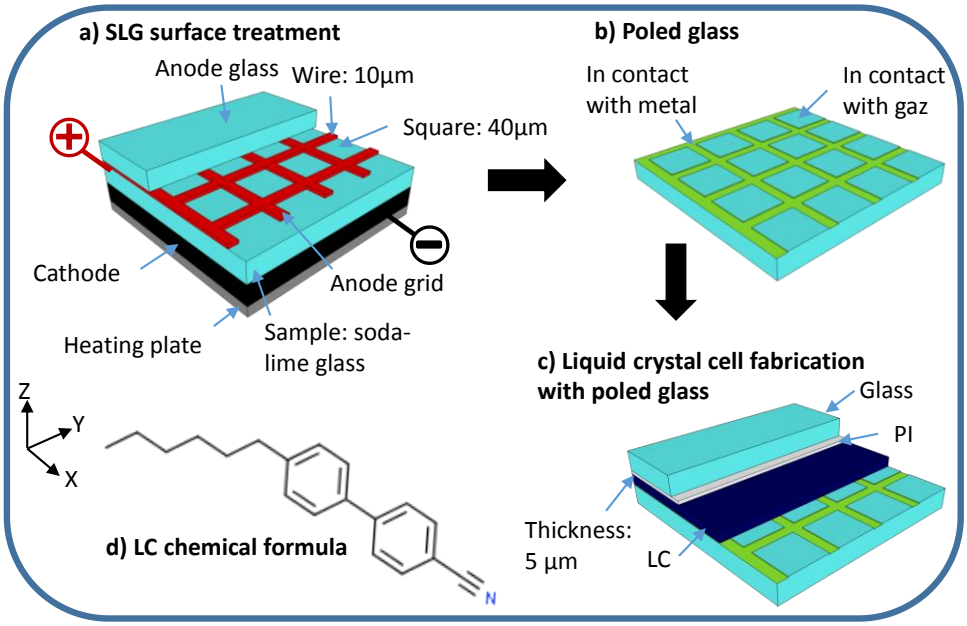

Figure 1. Schematics of LC cell fabrication steps: (a) thermo-electrical imprinting treatment, (b) Extraction of the patterned SLG substrate (c) LC cell conception formed of the assembly of the poled SLG surface with a homeotropic PI coated glass. The 5µm thick cell is then filled with 4'-hexyl-biphenylcabonitrile LCs ((d) LC chemical formula).

Before to characterize the poled glass surface and finally the LC cell, one should note the peculiarities of this thermo-electrical process by pointing out the generation of DC plasma occurring at the vicinity of the electrode edges and the glass surface. A video of localized plasma emissions has been recorded during the poling treatment using a 50x microscope objective that allows to observe the location and the dynamic of these DC gas discharges (see **Visualization 1** for the complete video). In **Figure 2(a)** and **(b)**, we have depicted respectively a picture of the nickel grid used as anode and a "stacking" picture corresponding to 1 min of the plasma emission video. Plasma-assisted poling processes have been reported previously [30,36], similarly, we observe in the current study (i) the same spectral emission from second positive system (SPS) electronic transition of N_2 ($C^3\,\Pi_u \rightarrow B^3\,\Pi_g$) [28] and (ii) a good correlation between temporal evolutions of electrical current and plasma emission (**Figure 2(c)**). It points out the importance of the gaz discharges in the mechanisms of charge carrier displacements during the polarization process. Moreover, as depicted in **Figure 2(b)**, the plasma emission is managed spatially by the electrode pattern which denotes the respective spatial control of surface electrical currents through gas discharges.

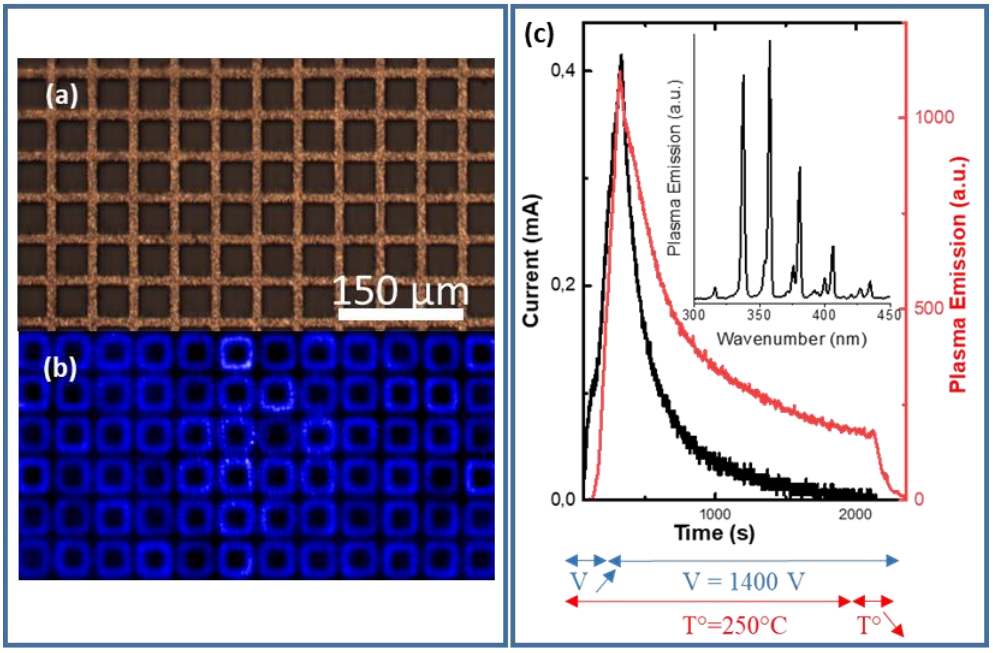

Figure 2. (a) anode picture before poling from the top, (b) "stacking" picture of 1 min of the plasma video during poling (see **Visualization 1**) and (c) recorded electrical current and plasma emission intensity during poling in function of time. The voltage increases with a slope of 280 V/min, reaching the target value of 1400 V at 300 sec and is constant until the end of the treatment, the temperature decrease at 2150 sec. On the inset is reported the emission spectrum measured within 300-450 nm spectral range.

3. Results

3.1 Glass composition and second harmonic generation response of the micro structured poled glass surface.

As reminded in the introduction, the main expected effects of such thermo-electrical polarization process concern (i) the formation of a mobile cations depletion and structural changes of the glassy matrix and (ii) the implantation of frozen charges and static electrical fields. [37–43] These process outcomes on the glass surface properties were respectively characterized by Energy-dispersive X-ray (EDX) spectroscopy and SHG polarized imaging.

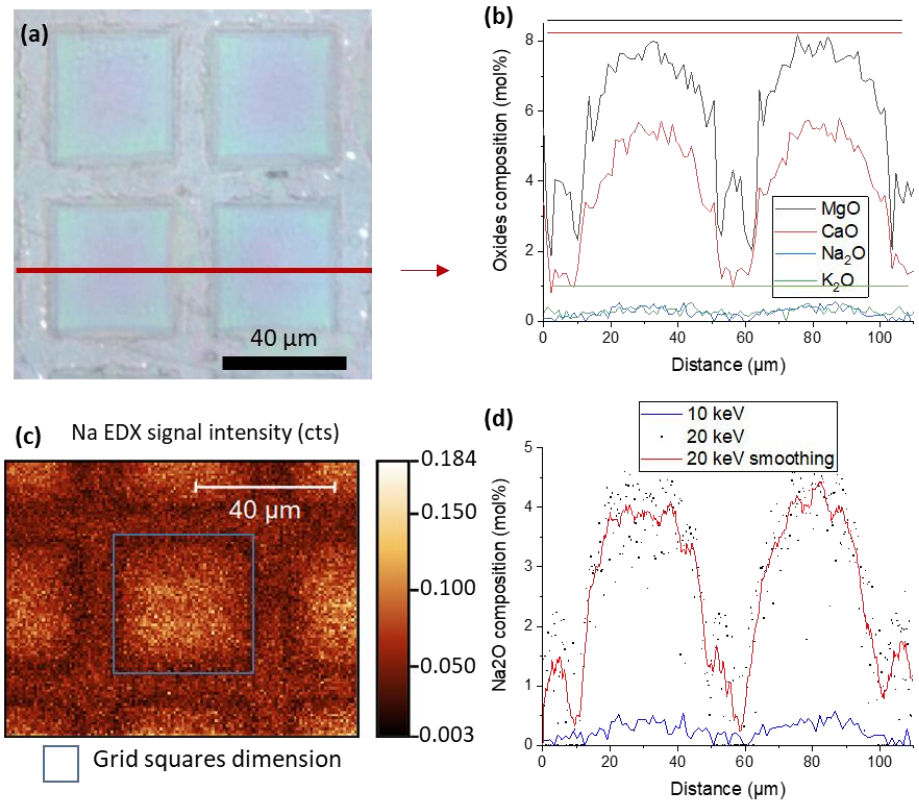

Figure 3. a) Observation of the surface after poling with an optical microscope. EDX characterisations: b) cation oxide concentration profiles for a beam energy of 10 keV, the straight lines materializing the initial oxide concentrations, [Na_2O] = 15,45 mol%, [MgO] = 8,44 mol%, [CaO] = 8,09 mol%, [K_2O] = 0,82 mol%, c) mapping representing Na EDX signal (arbitrary units in counts (cts)) and d) Na_2O composition quantification with different electron beam energies, the 20keV smoothing is calculated by adjacent averaging method, with a window size of 10 points.

In **Figure 3 (a)**, we show the imprinted glass surface observed with an optical microscope. The zones in contact with the grid have a rather uniform aspect with some topological defects linked to the influence of the grid roughness on the imprinting process [25]. The inner part of the patterns, corresponding to the location of the plasma discharges, presents an iridescence linked to refractive index variations as reported in one of our previous study [44]. **Figure 3 (b)** contains the alkaline and alkaline earth oxides composition profiles measured with a 10 keV electron beam whereas in **Figure 3 (d)** we focus on the sodium oxide composition measured with respectively 10 and 20 keV electron beams. Adjusting the electron beam energy allows to probe different thicknesses of the polarized surface. By assuming a uniform density of the glass matrix ($\rho = 2.53$ g/cm^3), the probed thicknesses have been estimated to 1.21 µm at 10 KeV and 3.88 µm at 20 KeV. [45]

At 10 KeV, the Na_2O and K_2O concentrations are always measured below 0.5 mol% for the whole surface. As the initial glass composition contains 15.45 mol% of Na_2O and 0.8 mol% of K_2O, it points out the complete alkaline ions depletion occurring at the surface. Concerning the alkaline earth oxides, at 10 KeV their concentration profiles show large variations with a

strong concentration gradient at the boarder of the square which reach a plateau in the middle of the square patterns. A similar trend is observed for the Na_2O profile probed at 20 KeV. A mapping of the Na_2O concentration measured for a 20 keV electron beam (**Figure 3 (c)**) reveals the poling induced spatial gradients of mobile cations concentrations which patterns follow accurately the electrode geometry. The thickness of the sodium depletion layer is maximum at the electrode/glass surface contact area and decrease gradually from the electrode edge towards the center of the square patterns. If one compare these results to other micro-poling studies using patterned thin films as anode electrodes (metallic or ITO 100 nm-thick films) [27–29,31,33,44], the main difference concerns the spatial effects of the polarization treatment, i.e. the location of the induced depletion in mobile ions. In these previous studies using thin films as anode, the depletion is no more effective few micrometers out of the electrode contact zones. One could explain such difference by the larger thickness of the nickel grid anode (4 µm) that allows for localized plasma generation thanks to a sufficient quantity of gas within the volumes formed by the micrometric grid. This localized gaz discharges permit to carry surface electrical currents, which considerably extend the in-plane polarization effects and thus allow the imprinting process to be effective on the entire glassy surface.

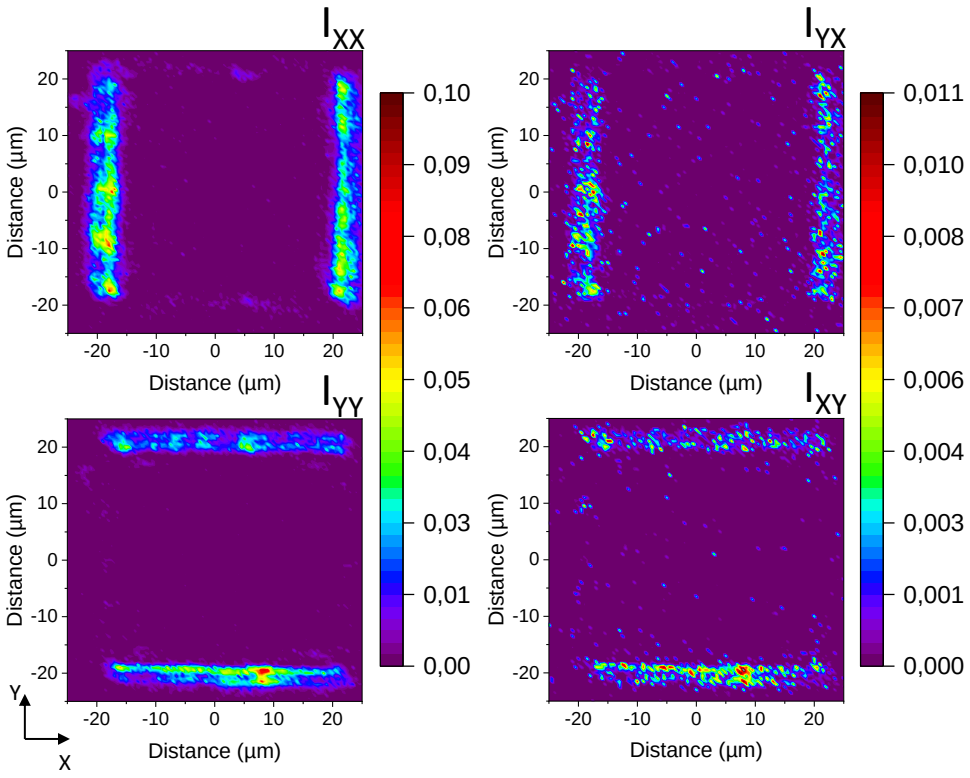

Figure 4. Polarized SHG intensity image of the poled glass surface centered on a square.

The second technique dedicated to the micro-poled surface characterization is SHG polarized microscopy. This technique is sensible to any loss of centrosymmetry induced by the

polarization process on the glass matrix. SHG imaging of the polarized glass surface was achieved in reflection (epifluorescence) mode with four linear state configurations of light polarization. All technical details are available in the experimental section, but one should remind that the incident laser beam is focused on the poled glass surface with a numerical aperture of 0.40 and a linear incident polarization oriented either along the X or Y axis chosen to be parallel to the square patterns directions. Similarly, either the X or Y linear polarization of reflected SHG signals are analyzed. It forms a combination of four images of SHG intensity (I_{XX}, I_{YY}, I_{XY} and I_{YX} ; the first and second indexed letters correspond respectively to the incident light polarization and the SHG analyzed polarization). Note a SHG intensity image I_{IJ} (I, J= X, Y) probe the second-order susceptibility $\chi^{(2)}_{J;II}$. Such analysis allows a complete characterization of the in-plane components of the second order optical susceptibility tensor, $\chi^{(2)}$, originating from the in-plane poling effects on the glassy surface. **Figure 4** shows the four polarized SHG images of a 50 µm wide zone centered on an imprinted square pattern. The SHG signals are located at the borders of the square pattern corresponding to the edges of the anode grid and are highly dependent on both incident light and SHG polarization states. By comparing intensities of SHG in parallel and crossed light polarization configuration, we observe that the terms $\chi^{(2)}_{X;XX}$ and $\chi^{(2)}_{X;YY}$ are maximum for a pattern orientation along the Y axis and null along the X axis. Similarly, $\chi^{(2)}_{Y;YY}$ and $\chi^{(2)}_{Y;XX}$ are maximum for a pattern orientation along the X axis and null along the Y axis. Moreover, one has to notice the high similarity of the SHG images measured with the same SHG polarization state. Such spatial correspondence allows evaluating polarization ratio (i.e. I_{XX}/I_{YX} and I_{YY}/I_{XY}) which are found to be close to 9 (±10%) for all SHG active zones. These observations point out the following links between the patterned $\chi^{(2)}$ components: $\chi^{(2)}_{X;XX} = 3.\chi^{(2)}_{X;YY}$ and $\chi^{(2)}_{Y;YY} = 3.\chi^{(2)}_{Y;XX}$. As expected from previous studies [21,39], this is in accordance with an electro optical origin of the poling induced loss of centrosymmetry for which the second order optical response originates from an interaction between a static electrical field, E_{stat}, and the third order susceptibility of an isotropic media, $\chi^{(3)}$, in other words: $\chi^{(2)} = 3.\chi^{(3)}.E_{stat}$ [41,46].

Finally, this polarized SHG characterization put in evidence the spatial patterning of multi-component electric fields which in-plane orientation and location are accurately controlled. These spatially controlled polarization effects should be linked to the directional control of surface electrical current during the thermo-electrical polarization process, which allows to manage the geometry of both charge gradients and frozen static fields.

3.2 Characterization of the liquid crystal multi domain alignments

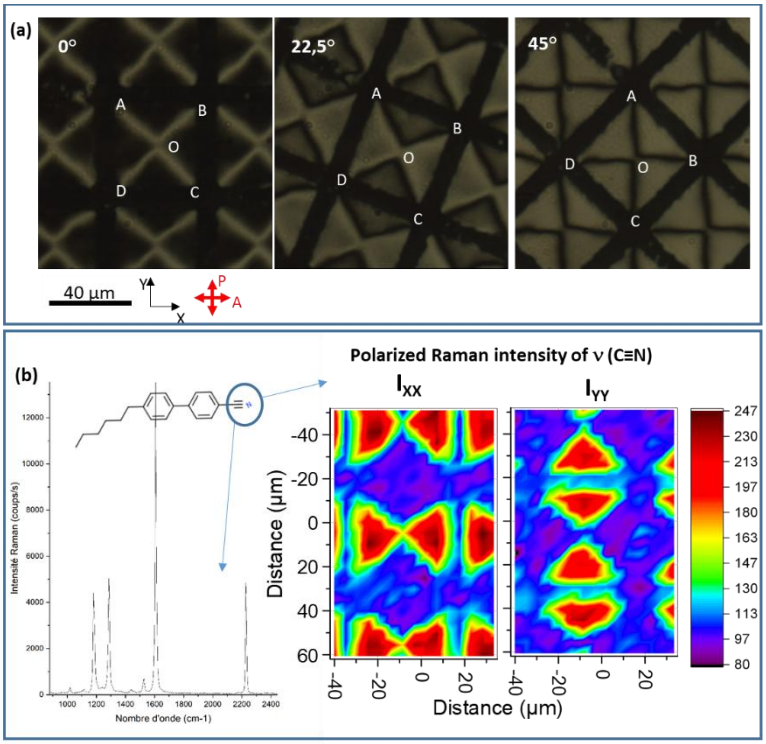

Figure 5. (a) Observations between crossed polarizers of the LC cell for various rotation angles, A and P arrows respectively symbolize directions of the analyzer and polarizer. **(b)** Polarized Raman spectra of the liquid crystal 4'-hexyl-biphenylcabonitrile molecule, Raman mapping of the C≡N triple bond stretching mode with incident and analyzed polarization state either along the X or Y axis.

After the characterization of the poled glass surface, the LC cell is fabricated as shown in **Figure 1c**. **Figure 5** shows pictures of the cell examined between crossed polarizers for an orientation of 0°, 22.5° and 45°, the observations for 90° and 67.5° are respectively similar to the first two. There is a strong dependence of the light transmission with the LC cell rotation, which can lead to LC orientation deduction. At 0°, the cross polarizer are parallel to the square pattern directions, the aspect of the cell is dark, except a white cross along the diagonals AC and BD. For a rotation of 22.5°, the parts corresponding to the contact area with the anode grid during the poling process stay dark, the brightness increase inside four triangular domains formed by the cross (ABO, BCO, CDO, ADO), the brightness of the cross formed by the diagonal lines decrease. At 45°, the brightness in the four triangles is equal and maximum, the parts forming the contour of the square pattern stay dark. These observations demonstrate that (i) the LC alignment is homeotropic along the square pattern i.e. the glass surface that was in direct contact with the anode grid and (ii) inside the square patterns, i.e. at

the location of the plasma discharges during the poling process, the LC alignment is planar. The triangular domains observed in this zone corresponds to planar alignments either parallel or perpendicular to the borders of the squares. To complete the molecular alignment description, we have carried out Raman polarized imaging characterizations, as Raman spectroscopy is well known to be sensitive to LC orientations [47–50]. The Raman spectra of the molecule used in this work (**Figure 5 (b**)) shows four strong bands which can be identify to: C-H in-plane bending vibration at 1175 cm^{-1}, inter-ring C-C stretching at 1280 cm^{-1}, benzene-ring stretching at 1606 cm^{-1} and C≡N stretching at 2226 cm^{-1}. [51] The 4'-hexyl-biphenylcabonitrile's triple bond C≡N leans toward the molecule axis and its stretching mode is known to be an accurate probe of the LC alignment by Raman methods [47,50]. Thus, two Raman intensity images of the C≡N stretching using polarization state of both incident laser and analyzed Raman (called also parallel polarization $I_{//}$) either along the X or Y laboratory axis (noted I_{XX} and I_{YY}) are shown in **Figure 5 (b)**.

The triangular domains with planar orientations are clearly observed by Raman imaging. The triangles pointing up or down towards the square centers are seen in the I_{YY} polarization configuration. Inversely, triangles pointing horizontally towards the middle of the patterned squares are observed for the I_{XX} Raman map. Of course, these results are consistent with the data obtained by observations with a pair of crossed polarizers. But they allow to precise that inside the triangular domains, LCs have a planar orientation perpendicular to the closer border of the square. One should also notice that for all triangular domains depicted in **Figure 5**, their optical responses are identical showing the same degree of alignment. These domains differ only by the in-plane orientation of their optical axis that appears to be dictated by the patterned glass surface.

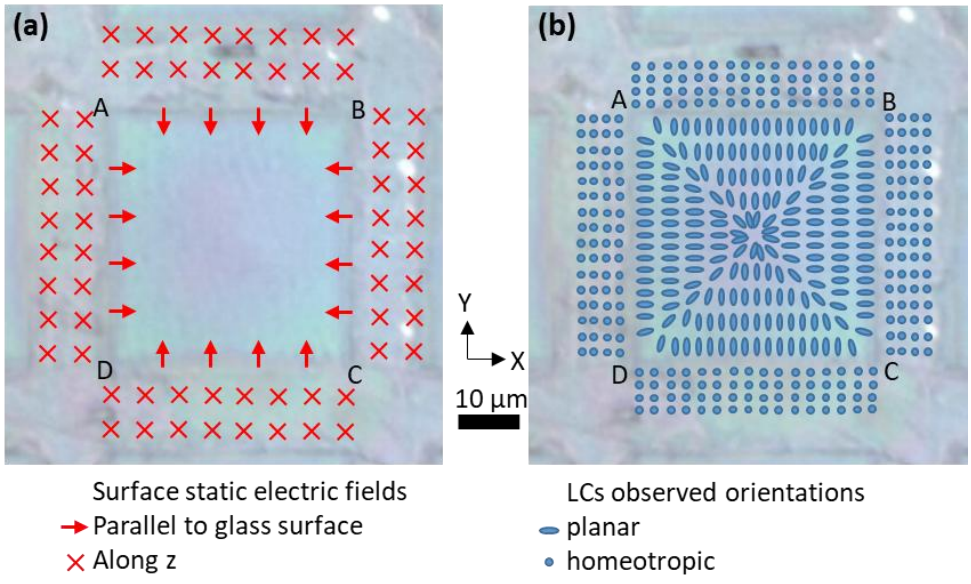

Figure 6. Schematic representation of a) static electrical fields implanted at the glass surface and b) LC alignments.

Finally, one needs to correlate the formation of LC multi domain of alignments with the polarized glass surface characterizations detailed above. One key observation of this study concerns the surface electrical field characterized by SHG measurements that appear to be accurately linked to the LCs planar alignments observed within the triangular domains formed in the square patterns. Similarly, for the areas forming the contour of the square patterns, the homeotropic LC orientation observed should be linked to an expected static field perpendicular to the surface due to its location at the contact zone with the anode grid during the poling process. Unfortunately, the out of plane electro optical response cannot be characterized by SHG microscopy using linear light polarization as carried out in this study. Nevertheless, such out of plane field components have been reported many times for classical planar electrodes using an adapted SHG Maker Fringes characterization method [39] or by SHG microscopy using radial polarization state of the incident laser and high numerical aperture objectives [27,28]. To summarize this correlation, in **Figure 6** schematic representations of both static field components deduced from SHG measurements and LCs orientations are depicted. The static fields frozen within the sub surface of the glassy matrix induce uniform LC alignment parallel to their direction. At the boundary lines formed by the polarized pattern, the planar components of the static fields are maximum, which further guide the LCs planar alignment towards the middle of the patterned squares.

As a last comment, one should put an emphasis on the importance of surface electrical currents promoted by plasma discharges extending considerably the in-plane polarization effects. One should note that poling conditions without surface plasma ignitions (using patterned thin films as anode electrodes) did not permit to induce efficient LC alignments. This point supports that it is essential to polarize the entire glass surface using long range in-plane poling effects for an accurate control of LC alignments. They might be at the origin of other surface mechanisms influencing the LC alignment. One can suppose the existence of some very weak poling-induced surface anisotropy which could not be observed with the characterization tools used in this study. Additionally, the surface charge density induced along the entire glass surface is expected to modify the surface energy [7,40,52] and influence the LC surface anchoring mechanisms. Further experiments are in progress to tackle these assumptions.

4. Conclusion

Static electric fields can be imprinted on a commercial silicate glass by a thermo-electrical polarization process enabling an accurate spatial programming of LCs orientation, including the formation of complex multi domain alignments. The orientation of static fields, implanted at the surface of the glass substrate, were characterized by polarized SHG imaging and a clear correlation between LC alignments (characterized by polarized micro-Raman imaging) and both location and direction of implanted fields has been shown. The presence of plasma discharges allows extending the surface electrical currents enabling polarization effects on the whole surface with an accurate directional control. This study is a new proof of concept demonstrating that an accurate control of LC organization can be achieved by managing glass surface electrical properties. We think that this new surface electrical functionality has significant potential for the fabrication of next generation of LC devices.

5. Experimental Section/Methods

LC cell preparation:

The glass used was a 1 mm thick slide of a commercially available soda lime glass (SLG) with a composition of 72.20 wt% SiO_2, 14.30 wt% Na_2O, 6.40 wt% CaO, 4.30 wt% MgO, 1.20 wt% K_2O, and 1.20 wt% Al_2O_3. A sample has been washed by solvents in ultrasound baths before to be poled with a nitrogen atmosphere at normal pressure and an atmospheric

humidity lower than 1 %. The anode used is a nickel grid composed of 10 µm wide wires and 40 µm wide squares as shown in Figure 1a; the thickness of the grid is 4 µm. At the other side, a piece of silicon wafer was used as the cathode. All the system was heated to 250 °C and a voltage of 1400 V was then applied during 30 min. In the meanwhile, an acquisition of a video with a camera connected to an objective of 50x (NA = 0,42) has been done to record plasma emissions.

After having characterized the surface, the poled substrate is assembled with a soda-lime glass coated with a homeotropic polyimide (PI) using a UV curing glue and silica balls as spacers to constitute a 5 µm thick cell (Figure 1c). The cell is then filled with a liquid crystal composed of the molecule 4'-hexyl-biphenylcabonitrile (Figure 1d) sold by Merck.

Characterization:

A scanning electron microscopy Quanta FEI system coupled with an energy-dispersive x-ray spectroscopy detector (EDX) is used to quantify the atomic composition at the surface of the sample.

Polarized SHG images were recorded with a µ-SHG XY scanning system by optical microscopy combined with SHG spectroscopy on a custom-built scanning SHG microscope developed at the ISM lab [53,54]. The excitation source used was a 1064 nm picosecond laser (Leukos Opera), which delivers 50 ps pulses at a repetition rate of 1 MHz. The laser incident light was set at an average power of 300 mW and focused into the sample with a near-IR 20 × objective (Mitutoyo M-PLAN APO, NA 0.4), and the resultant SHG at 532 nm was collected in the backward direction (epifluorescence mode) using a photomultiplier tube. Large polarized SHG images of 50 × 50 µm2 where recorded with a spatial resolution of 1 µm.

The first LC characterization method was transmission optical microscopy with a pair of crossed polarizers: a microscope with a 50x (NA = 0.42) objective is used to observe the LC cell placed in the XY plane, transmitted white light propagated along the Z axis, the analyzer and polarizer being respectively parallel to X and Y. The cell was then rotated along the Z axis. Second, we used a micro-Raman HR800 (Horiba/Jobin-Yvon) spectrometer with a 532 nm CW laser as source in the backscattering geometry at room temperature, the spectral resolution was 2.5 cm^{-1}. The liquid crystal cell was placed in XY plane and laser beam propagated along Z. Two polarized Raman maps were measured, using variable polarizations of both incident laser and analyzed Raman scattering either along X or Y directions.

Funding

This study has received financial support from the Canadian NSERC (05888) and CRC (230212) as well as French State in the framework of the Investments for the Future programme IdEx université de Bordeaux / GPR LIGHT. The authors gratefully acknowledge the financial support from the CNRS project EMERGENCE @INC2019. This project has received funding from the European Union's Horizon 2020 research program under the Marie SkłodowskaCurie grant agreement no. 823941 (FUNGLASS), from the Conseil Régional Aquitaine (IR Funglass) and from the Agence Nationale de la Recherche (Proteus). The Raman experiments were conducted using the SIV platform at the University of Bordeaux founded by the FEDER and the Region Aquitaine.

Data availability

Data underlying the results presented in this paper are not publicly available at this time but may be obtained from the authors upon reasonable request.

Disclosures

The authors declare no conflict of interest.

References

1. D.-K. Yang, *Fundamentals of Liquid Crystal Devices* (Wiley-SID Series in Display Technology, 2014).
2. V. Chigrinov, "Photoaligning and Photopatterning — A New Challenge in Liquid Crystal Photonics," Crystals **3**, 149–162 (2013).
3. P. G. de Gennes and J. Prost, *The Physics of Liquid Crystals*, Second Edition, International Series of Monographs on Physics (Oxford University Press, 1995).
4. Y. Zhu, L. Wang, Z. Lu, Y. Wei, X. X. Chen, and J. H. Tang, "Atomic force microscopic study of rubbed polyimide films," Appl. Phys. Lett. **65**, 49–51 (1994).
5. Y. B. Kim, H. Olin, S. Y. Park, J. W. Choi, L. Komitov, M. Matuszczyk, and S. T. Lagerwall, "Rubbed polyimide films studied by scanning force microscopy," Appl. Phys. Lett. **66**, 2218–2219 (1995).
6. Y. Xia, A. Honglawan, and S. Yang, "Tailoring surface patterns to direct the assembly of liquid crystalline materials," Liquid Crystals Reviews **7**, 30–59 (2019).
7. F. Lind, D. Palles, D. Möncke, E. I. Kamitsos, and L. Wondraczek, "Modifying the surface wetting behavior of soda-lime silicate glass substrates through thermal poling," Journal of Non-Crystalline Solids **462**, 47–50 (2017).
8. A. J. Hess, Q. Liu, and I. I. Smalyukh, "Optical patterning of magnetic domains and defects in ferromagnetic liquid crystal colloids," Appl. Phys. Lett. **107**, 071906 (2015).
9. Y. Guo, M. Jiang, C. Peng, K. Sun, O. Yaroshchuk, O. Lavrentovich, and Q.-H. Wei, "High-Resolution and High-Throughput Plasmonic Photopatterning of Complex Molecular Orientations in Liquid Crystals," Advanced Materials **28**, 2353–2358 (2016).
10. J.-H. Kim, M. Yoneya, J. Yamamoto, and H. Yokoyama, "Nano-rubbing of a liquid crystal alignment layer by an atomic force microscope: a detailed characterization," Nanotechnology **13**, 133–137 (2002).
11. J.-H. Kim, M. Yoneya, and H. Yokoyama, "Tristable nematic liquid-crystal device using micropatterned surface alignment," Nature **420**, 159–162 (2002).
12. D. Qin, Y. Xia, and G. M. Whitesides, "Soft lithography for micro- and nanoscale patterning," Nat Protoc **5**, 491–502 (2010).
13. K. Takatoh, M. Hasegawa, M. Koden, N. Itoh, R. Hasegawa, and M. Sakamoto, *Alignment Technologies and Applications of Liquid Crystal Devices* (Taylor & Francis, 2005).
14. M. Schadt, H. Seiberle, and A. Schuster, "Optical patterning of multi-domain liquid-crystal displays with wide viewing angles," Nature **381**, 212–215 (1996).
15. J.-H. Park, T.-Y. Yoon, W.-J. Lee, and S.-D. Lee, "Multi-domain Liquid Crystal Display with Self-Aligned 4-Domains on Surface Relief Gratings of Photopolymer," Mol. Crystals & Liquid Crystals **375**, 433–440 (2002).
16. J.-H. Park, Y. Choi, T.-Y. Yoon, C.-J. Yu, and S.-D. Lee, "A self-aligned multi-domain liquid-crystal display on polymer gratings in a vertically aligned configuration," J. Soc. Inf. Display **11**, 283 (2003).
17. X. Zhao, A. Bermak, F. Boussaid, T. Du, and V. G. Chigrinov, "High-resolution photoaligned liquid-crystal micropolarizer array for polarization imaging in visible spectrum," Opt. Lett. **34**, 3619 (2009).
18. B. Wei, W. Hu, Y. Ming, F. Xu, S. Rubin, J. Wang, V. Chigrinov, and Y. Lu, "Generating Switchable and Reconfigurable Optical Vortices via Photopatterning of Liquid Crystals," Adv. Mater. **26**, 1590–1595 (2014).
19. G. Goubert and T. V. Galstian, "Light Controlled Capillarity of Liquid Crystals on Photo Anisotropic Surfaces," Molecular Crystals and Liquid Crystals **526**, 46–57 (2010).
20. S. R. Nersisyan, N. V. Tabiryan, D. M. Steeves, B. R. Kimball, V. G. Chigrinov, and H. S. Kwok, "Study of azo dye surface command photoalignment material for photonics applications," Appl. Opt. **49**, 1720 (2010).
21. R. A. Myers, N. Mukherjee, and S. R. J. Brueck, "Large second-order nonlinearity in poled fused silica," Opt. Lett. **16**, 1732 (1991).
22. G. Wallis and D. I. Pomerantz, "Field Assisted Glass- Metal Sealing," Journal of Applied Physics **40**, 3946–3949 (1969).
23. P. Nitzsche, K. Lange, B. Schmidt, S. Grigull, U. Kreissig, B. Thomas, and K. Herzog, "Ion Drift Processes in Pyrex- Type Alkali- Borosilicate Glass during Anodic Bonding," J. Electrochem. Soc. **145**, 1755–1762 (1998).
24. M. Dussauze, E. I. Kamitsos, E. Fargin, and V. Rodriguez, "Structural Rearrangements and Second-Order Optical Response in the Space Charge Layer of Thermally Poled Sodium−Niobium Borophosphate Glasses," J. Phys. Chem. C **111**, 14560–14566 (2007).
25. L. A. H. Fleming, D. M. Goldie, and A. Abdolvand, "Imprinting of glass," Opt. Mater. Express **5**, 1674 (2015).
26. M. Dussauze, E. I. Kamitsos, E. Fargin, and V. Rodriguez, "Refractive index distribution in the non-linear optical layer of thermally poled oxide glasses," Chemical Physics Letters **470**, 63–66 (2009).
27. L. Karam, F. Adamietz, V. Rodriguez, F. Bondu, A. Lepicard, T. Cardinal, E. Fargin, K. Richardson, and M. Dussauze, "The effect of the sodium content on the structure and the optical properties of thermally poled sodium and niobium borophosphate glasses," Journal of Applied Physics **128**, 043106 (2020).

28. L. Karam, F. Adamietz, D. Michau, C. Gonçalves, M. Kang, R. Sharma, G. S. Murugan, T. Cardinal, E. Fargin, V. Rodriguez, K. A. Richardson, and M. Dussauze, "Electrically Micro- Polarized Amorphous Sodo- Niobate Film Competing with Crystalline Lithium Niobate Second- Order Optical Response," Adv. Optical Mater. **8**, 2000202 (2020).
29. R. Alvarado, L. Karam, R. Dahmani, A. Lepicard, F. Calzavara, A. Piarristeguy, A. Pradel, T. Cardinal, F. Adamietz, E. Fargin, M. Chazot, K. Richardson, L. Vellutini, and M. Dussauze, "Patterning of the Surface Electrical Potential on Chalcogenide Glasses by a Thermoelectrical Imprinting Process," J. Phys. Chem. C **124**, 23150–23157 (2020).
30. M. Chazot, M. Paraillous, S. Jouannigot, L. Teulé- Gay, J. Salvetat, F. Adamietz, R. Alvarado- Meza, L. Karam, A. Poulon, T. Cardinal, E. Fargin, and M. Dussauze, "Enhancement of mechanical properties and chemical durability of Soda- lime silicate glasses treated by DC gas discharges," J. Am. Ceram. Soc. **104**, 157–166 (2021).
31. A. Lepicard, T. Cardinal, E. Fargin, F. Adamietz, V. Rodriguez, K. Richardson, and M. Dussauze, "Micro-structuring the surface reactivity of a borosilicate glass via thermal poling," Chemical Physics Letters **664**, 10–15 (2016).
32. A. N. Kamenskii, I. V. Reduto, V. D. Petrikov, and A. A. Lipovskii, "Effective diffraction gratings via acidic etching of thermally poled glass," Optical Materials **62**, 250–254 (2016).
33. A. Lepicard, F. Adamietz, V. Rodriguez, K. Richardson, and M. Dussauze, "Demonstration of dimensional control and stabilization of second harmonic electro-optical response in chalcogenide glasses," Opt. Mater. Express **8**, 1613 (2018).
34. M. Dussauze, V. Rodriguez, F. Adamietz, G. Yang, F. Bondu, A. Lepicard, M. Chafer, T. Cardinal, and E. Fargin, "Accurate Second Harmonic Generation Microimprinting in Glassy Oxide Materials," Advanced Optical Materials **4**, 929–935 (2016).
35. Z. Rajaofara, P. Leproux, M. Dussauze, A. Tonello, V. Rodriguez, L. Karam, H. Kano, J.-R. Duclére, and V. Couderc, "Mapping the second and third order nonlinear susceptibilities in a thermally poled microimprinted niobium borophosphate glass," Opt. Mater. Express **11**, 3411 (2021).
36. T. Cremoux, M. Dussauze, E. Fargin, T. Cardinal, D. Talaga, F. Adamietz, and V. Rodriguez, "Trapped Molecular and Ionic Species in Poled Borosilicate Glasses: Toward a Rationalized Description of Thermal Poling in Glasses," J. Phys. Chem. C **118**, 3716–3723 (2014).
37. Y. Quiquempois, N. Godbout, and S. Lacroix, "Model of charge migration during thermal poling in silica glasses: Evidence of a voltage threshold for the onset of a second-order nonlinearity," Phys. Rev. A **65**, 043816 (2002).
38. M. Dussauze, "Génération de second harmonique dans des verres borophosphate de sodium et niobium par polarisation thermique," (2005).
39. M. Dussauze, T. Cremoux, F. Adamietz, V. Rodriguez, E. Fargin, G. Yang, and T. Cardinal, "Thermal Poling of Optical Glasses: Mechanisms and Second-Order Optical Properties," Int J Appl Glass Sci **3**, 309–320 (2012).
40. T. Crémoux, "Physico-chimie aux interfaces de systèmes vitreux à charge d'espace," Université Bordeaux 1 (2013).
41. A. Lepicard, "Design of surface chemical reactivity and optical properties in glasses," (2016).
42. C. McLaren, M. Balabajew, M. Gellert, B. Roling, and H. Jain, "Depletion Layer Formation in Alkali Silicate Glasses by Electro-Thermal Poling," J. Electrochem. Soc. **163**, H809–H817 (2016).
43. C. McLaren, B. Roling, R. Raj, and H. Jain, "Mechanism of electric field-induced softening (EFIS) of alkali silicate glasses," Journal of Non-Crystalline Solids **471**, 384–395 (2017).
44. A. Lepicard, F. Bondu, M. Kang, L. Sisken, A. Yadav, F. Adamietz, V. Rodriguez, K. Richardson, and M. Dussauze, "Long-lived monolithic micro-optics for multispectral GRIN applications," Sci Rep **8**, 7388 (2018).
45. J. I. Goldstein, D. E. Newbury, P. Echlin, D. C. Joy, C. Fiori, and E. Lifshin, *Scanning Electron Microscopy and X-Ray Microanalysis* (Springer US, 1981).
46. P. G. Kazansky and P. St. J. Russel, "Thermally poled glass: frozen-in electric field or oriented dipoles?," Optics Communications **110**, 611–614 (1994).
47. A. N. Davies, W. Jeremy Jones, and A. H. Price, "Non-linear Raman spectroscopy of liquid crystals: Polarization measurements and relaxation processes in 4-cyano-4′-heptylbiphenyl (7CB)," J. Raman Spectrosc. **25**, 521–529 (1994).
48. S. Jen, N. A. Clark, P. S. Pershan, and E. B. Priestley, "Raman Scattering from a Nematic Liquid Crystal: Orientational Statistics," Phys. Rev. Lett. **31**, 1552–1556 (1973).
49. S. Jen, N. A. Clark, P. S. Pershan, and E. B. Priestley, "Polarized Raman scattering studies of orientational order in uniaxial liquid crystalline phases," The Journal of Chemical Physics **66**, 4635–4661 (1977).
50. K. Miyano, "Raman depolarization ratios and order parameters of a nematic liquid crystal," The Journal of Chemical Physics **69**, 4807–4813 (1978).
51. T. Morikawa, E. Shirai, J. Tanno, H. Takanashi, A. Yasuda, and K. Itoh, "Time-resolved Total Internal Reflection Raman Scattering Study on Electric-Field-Induced Reorientation Dynamics of Nematic Liquid Crystal of 4-Hexyl-4′-Cyanobiphenyl," Molecular Crystals and Liquid Crystals Science and Technology. Section A. Molecular Crystals and Liquid Crystals **312**, 69–94 (1998).

52. F. Mugele and J.-C. Baret, "Electrowetting: from basics to applications," J. Phys.: Condens. Matter **17**, R705–R774 (2005).
53. G. Gouget, M. Duttine, E. Durand, A. Villesuzanne, V. Rodriguez, F. Adamietz, T. Le Mercier, M.-D. Braida, and A. Demourgues, "Isolating the Two Room-Temperature Polymorphs of $NaNbO_3$: Structural Features, Optical Band Gap, and Reactivity," ACS Appl. Electron. Mater. **1**, 513–522 (2019).
54. M. Chazot, C. Arias, M. Kang, C. Blanco, A. Kostogiannes, J. Cook, A. Yadav, V. Rodriguez, F. Adamietz, D. Verreault, S. Danto, T. Loretz, A. Seddon, D. Furniss, K. Schepler, M. C. Richardson, and K. A. Richardson, "Investigation of ZnSe stability and dissolution behavior in As-S-Se chalcogenide glasses," Journal of Non-Crystalline Solids **555**, 120619 (2021).